DESIGN OF A HIGH-Q, LOW-IMPEDANCE, GHZ-RANGE PIEZOELECTRIC MEMS RESONATOR

B. Antkowiak[1], J.P. Gorman[2], M. Varghese[1], D.J.D. Carter[1], A.E. Duwel[1]
[1]The Charles Stark Draper Laboratory, Cambridge, MA
[2]Massachusetts Institute of Technology, Cambridge, MA

Abstract **–** In this paper, we present useful modeling procedures intended to characterize and optimize MEMS resonator-filter designs. We address two major areas: (1) the impedance of the resonators as a function of frequency, assuming a given damping value, and (2) the numerical calculation of resonator Quality factor (Q) due to known damping mechanisms. The impedance calculation procedure is targeted towards piezoelectric MEMS resonators, while the Q calculations are more general. We show how these modeling approaches have been used to design and optimize our piezoelectric resonator for high Q and low impedance in the GHz frequency range.

I. INTRODUCTION

We report on the development of an acoustic piezoelectric MEMS resonator designed for high Q and low impedance in the ~700 MHz – 1.2 GHz frequency range. Processing of the aluminum nitride resonator is IC-compatible, offering the potential for integration in transceiver applications. Additionally, since the resonant frequency is defined by the *length* of the resonator, large arrays of resonators with different frequencies can be fabricated on one chip, offering the potential for more complex filter designs or fast frequency hopping applications.

The resonator is a longitudinal-mode, piezoelectrically-actuated device consisting of a sandwich of metal/aluminum-nitride/metal (**Figure 1**). It is suspended above a gap by two tethers. The device is a one-port component, where top and bottom metal electrodes both actuate the resonator and sense its response.

The resonator geometry, materials, and fabrication process are all designed with careful attention to the resulting *quality factor* and the electrical *impedance* of the device. To this end, new modeling and characterization approaches have been developed to quantify the resonator performance and optimize designs. The modeling results are presented, and generic methodologies are outlined for the benefit of future designs. Resonators are currently being fabricated so that detailed model predictions and optimizations can be experimentally verified.

II. Frequency Response Function

Coupled Piezoelectric-Mechanical Equations

The resonator performance as a filtering element is best evaluated by studying its impedance over a wide bandwidth of frequencies. The specific modeling goal is to develop an electrical frequency response function (FRF) using a finite-element (FE) based state-space model. The FRF is compared to analytical solutions of the simplified beam equations for a single resonance. The FE based approach has the benefit that the effects of other modes, fabricated asymmetries, and electrode placement can be evaluated thoroughly, which is not true of analytical models.

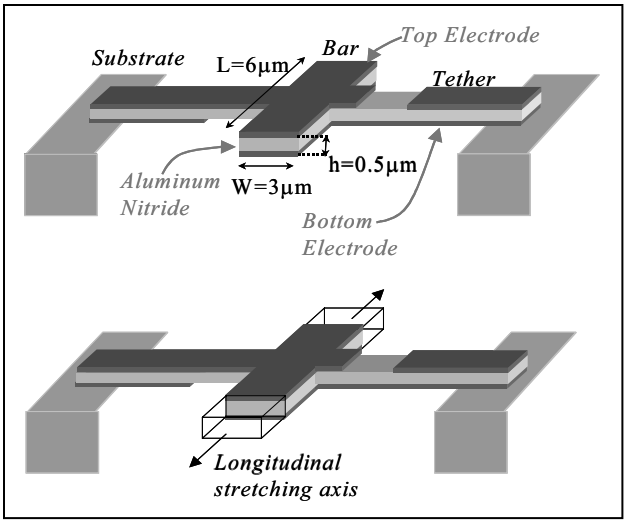

Figure 1: *Schematic of MEMS piezoelectric longitudinal bar resonator design. For dimensions shown above, the AlN bar has a resonant frequency of 780 MHz.*

In developing the device impedance model, we begin with the (lossless) coupled mechanical-piezoelectric equations:

$$(1)\quad \rho\ddot{\mathbf{u}} = \nabla\cdot\left(\mathbf{c}\nabla\mathbf{u} + \mathbf{e}^T\nabla\phi\right)$$

$$(2)\quad \nabla\cdot\left(\mathbf{e}\nabla\mathbf{u} - \boldsymbol{\varepsilon}\nabla\phi\right) = 0$$

where $\boldsymbol{u}$ is the displacement vector and ϕ is the scalar potential. (A complete list of variables is included in the Appendix). Equation (1) is based on force balance in the bulk, and boundary conditions capturing the size, shape, and support geometry must be applied. Equation (2) is based on Gauss's Law $\nabla\cdot\mathbf{D} = 0$ in a source-free material. In our case, where electrodes coat two boundaries, either fixed potential ϕ or fixed charge ($\hat{n}\cdot\mathbf{D} = \sigma_s$) conditions must be applied.

The electrostatic potential can be written as a superposition of solutions: $\phi^{(u)}$ which solves equation (2) with zero boundary conditions, and $\phi^{(BC)}$ which solves equation (2) with no piezoelectric term (*i.e.,* Laplace's equation) with fixed potential boundary conditions. In both the analytical and FE based models, we make the simplifying assumption that:

(3) $\phi = \phi^{(u)} + \phi^{(BC)} \approx \phi^{(BC)}$

This says that the potential is driven primarily by the applied voltage and not by the mechanical response. $\phi^{(BC)}$ drives the mechanical equation, so the piezoelectric effect is still included[1]. For isotropic permittivity, the resulting un-coupled system is:

(4) $\rho\ddot{\mathbf{u}} = \nabla \cdot \left(\mathbf{c}\nabla\mathbf{u} + \mathbf{e}^T \nabla\phi^{(BC)}\right)$

(5) $\varepsilon\nabla^2\phi^{(BC)} = 0$

The mechanical boundary conditions reflect the free-free bar geometry of our design. The electrical boundary conditions have $\phi = 0$ on the bottom electrode and $\phi = V_{in}$, the applied voltage, at the top electrode.

Although an exact solution to (5) should include fringing fields, for small gap-to-area $h/(L \cdot W)$ ratio, a good approximation is:

(6) $\phi^{(BC)} = V_{in} z / h$

This $\phi^{(BC)}$ is used as the driving force in (4). Although this force has a simple symmetry, it can still excite a multitude of mechanical modes. The linear combination of excited modes can be calculated, and the output current is calculated by:

(7) $\mathbf{D} = \mathbf{e}\nabla\mathbf{u} + \varepsilon\nabla\phi^{(BC)}$

(8) $Q_{out} = \int_{electrode} D \cdot dA$

(9) $I_{out} = \dot{Q}_{out}$

Frequency Response Function: Methodology

We have found that the use of a modal state-space model for (4), when applied to (7)-(9) leads to a simple V_{in}/I_{out} FRF. The first part of the procedure derives a standard mechanical (force-displacement) FRF as follows:

(a) Use any FE package to extract eigenvalues and eigenvectors of the bar.

(b) Choose a suitable set of eigenvectors and eigenvalues.

(c) Construct the matrix $[\Phi]$, where the columns Φ_i are eigenvectors. (Optional: Eliminate any non-essential physical degrees of freedom rows in $[\Phi]$.)

(d) The transformation of any state from physical displacement (u) to modal amplitudes (η) is then:

$\{u(\vec{x},t)\} = [\Phi]\{\eta(t)\}$.

(e) The mode amplitudes satisfy:

$\ddot{\eta}_i + 2\zeta_i\omega_i\dot{\eta} + \omega_i^2\eta_i = \widetilde{F}_i$,

where $\widetilde{F}_i$ is the force on the *i-th* mode, and ζ_i is a modal damping, assigned such that $Q_i = 1/2\zeta_i$.

(f) With the following substitution:

$$\{\beta\} = \begin{Bmatrix} \{\eta\} \\ \{\dot{\eta}\} \end{Bmatrix}$$

(g) equation (e) can be written as the first order system: (note [I] below is the identity matrix)

$\{\dot{\beta}\} = [A]\{\beta\} + [B]\{F\}$ where:

$$[A] = \begin{bmatrix} [0] & [I] \\ -[\omega^2] & -2[\zeta\omega] \end{bmatrix} \quad [B] = \begin{bmatrix} [0] \\ [\Phi]^T \end{bmatrix}$$

To go back to standard physical coordinates,

$\{u\} = [C]\{\beta\}$ where $[C] = [[\Phi] \quad [0]]$

(h) The FRF for the modal amplitudes is solved as:

$\{\beta(\omega)\} = [j\omega I - A]^{-1}[B]\{F(\omega)\}$.

(i) Finally, the FRF for the displacements is:

$\{u(x,\omega)\} = [H]\{F(\omega)\}$

with: $[H] = [C][j\omega I - A]^{-1}[B]$

Thus, given only the eigenvalues and eigenvectors of interest, a mechanical FRF is found. The procedure (a)-(g) is familiar in mechanical engineering [2] for formulating state-space models. This paper contributes an extension of the familiar method to include piezoelectric effects, as follows.

To get the current-voltage FRF, the force will be written in terms of V_{in}, and the output current is calculated from the charges induced by the linear combination of modal amplitudes.

For piezoelectrics, the force is related to applied potential by:

(10) $\mathbf{T}_{electric} = \mathbf{e}^T\nabla\phi$

[1] It can be shown that (3) is a good first order approximation [1]. The effect of the approximation is to neglect piezoelectric stiffening, which shifts the mechanical frequency slightly higher.

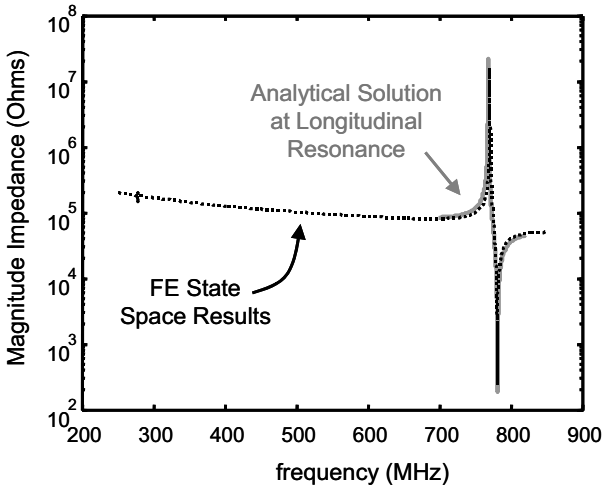

Figure 2: *Impedance FRF, based on FE state space model. Grey line shows analytical model results.*

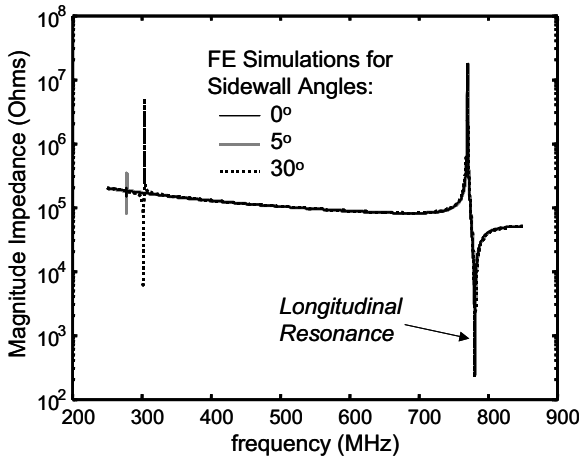

Figure 3: *Impedance FRF calculated from FE models. The effect of sloping the (0.5 um thick) sidewalls, due to processing, is explored.*

In our models, we use (6) for the potential and take the force at every node to be the element area (A_e) multiplied by the electric stress. For our models, then, we have:

$$(11)\quad \{F\} = A_e \left[e^T\right]\{0 \quad 0 \quad V_{in}/h\}^T$$

This can be directly substituted into (h) or (i).

The output current is calculated from (7)-(9). According to (7), the strain, rather than actual displacement is needed. A matrix operator, [Q], is constructed to find the strain vector from a displacement vector. In addition, the output charge is computed from a sum over the electrode area. For a given geometry, a matrix operator, [S], sums the displacement charges calculated only at the electrode nodes and takes the component perpendicular to the electrode area. Using these two constructed matrices, (7)-(9) combine with (h) to give the total charge:

$$(12)\quad Q_{out} = [S][e][Q][H]\{F(\omega)\}$$

Applying (9), we write:

$$(13)\quad I_{out} = Y(\omega)V_{in}$$

where

$$(14)\quad Y = j\omega[S][e][Q][H]\, A_e\left[e^T\right]\{0 \quad 0 \quad 1/h\}^T$$

Thus a set of matrix operations, based on the eigenvectors and eigenvalues of the mechanical system, is used to construct an electrical FRF. Since the quantities $\{\omega\}, [\Phi], [Q], \{\zeta\}, \text{and } [S]$ must be available, we found it convenient to construct the entire FE solution by hand. The software chosen was Mathcad, which is not optimized for complicated matrix inversions. However, the ease of use, combined with the fact that our geometry and desired mode could be modeled well with <100 nodes, allowed this choice. We compared the frequencies and mode shapes to those obtained with finer meshes in commercial packages, and found that the solutions matched to well within 10%.

FRF Results on RF Longitudinal Bar

Figure 2 shows the calculated impedance magnitude, $|Z|=|Y^{-1}|$ versus frequency. The magnitude is given in Ohms, for a 1 Volt input and assuming a modal damping corresponding to $Q=10^4$. The desired longitudinal resonance mode is number 16 and falls at 780 MHz. At resonance, the impedance drops down to approximately 200 Ohms (this value scales inversely proportional to Q).

Continuous beam equations with piezoelectric coupling have also been solved to find the Butterworth-van-Dyke circuit parameters at the longitudinal resonance. The details are not derived here, but are similar to those of many authors, including [3]. Although analytical solutions yield design intuition, the advantages to also developing the FE-based FRF are many – it takes into account all desired modes, covers a wide bandwidth, accounts for the electrode geometry and mode symmetries, and can include any complicated resonator geometry.

In the current design, the FE model was used to confirm that the electrode configuration was optimized for actuating and sensing the longitudinal mode, which is apparent in **Figure 2**. Although there are 15 lower mechanical modes, the desired longitudinal mode is the first to appear in $|Z(\omega)|$. (The nearest resonance in the FRF, not shown in Figure 2, is 18% higher in frequency). In addition, we explored how robust the design was to process imperfections such as sidewall angles. **Figure 3** shows impedance plots for 5^o and 30^o sidewall angles. For reference, our non-optimized dry etches of the Aluminum Nitride resonator bar have yielded sidewall angles of less than 15^o, and final angles of less than 5^o are realistic. From **Figure 3**, we see that the effect of sidewall angle is to introduce a lower mode response. However, the impedance amplitude of the spurious mode remains almost an order of magnitude higher than the longitudinal mode, even for a large 30^o sidewall angle.

III. THERMOELASTIC DAMPING SIMULATIONS

Both analytical and FE-based impedance models are derived assuming a given Q value. In the FE model, we assigned a modal damping that was not connected to any particular physics. In the analytical beam solutions, we used a viscous damping. The resulting Q value and material viscosity (ν) are related by [3]:

$$(15)\quad Q = E/\left(\nu 2\pi f_o\right)$$

with E as Young's modulus and f_o as the resonance frequency. For viscous damping, this relationship turns out to be true regardless of the mode shape or resonator geometry, although they are accounted for in f_o.

In most real physical systems, the material damping is not well described by a viscosity term. A more useful model is the standard anelastic model, where the constitutive stress-strain relationships are coupled to another internal degree of freedom. One of the most dominant mechanisms under study today in the MEMS resonator design area is thermoelastic damping [4-5]. This is the loss of energy through dissipative thermal currents, which are induced by mechanical strains. The coupled mechanical-thermal equations are [6]:

$$(16)\quad \rho\ddot{\mathbf{u}} = \nabla\cdot\left(\mathbf{c}\nabla\mathbf{u} - \mathbf{c}\boldsymbol{\alpha}T\right)$$

$$(17)\quad C_v\dot{T} = \nabla\cdot\boldsymbol{\kappa}\nabla T - T_o\boldsymbol{\alpha}\,\mathbf{c}\nabla\dot{\mathbf{u}}$$

Although analytical solutions to (16)-(17) are available [4,7-8], they can be obtained only for idealized geometries. The analytical approaches simplify the equations and solve for a subset of eigenvalues ω_i and eigenvectors Φ_i, with Q calculated by:

$$(18)\quad Q_i = \mathrm{Re}\{\omega_i\}/2\,\mathrm{Im}\{\omega_i\}$$

If an extra degree of freedom, temperature, is included at every node, then equations (16)-(17) can also be solved using a standard complex eigenvalues analysis. We have identified the software package Femlab®[2] as a useful platform for this analysis.

In the current study, the RF resonator geometry is a 3um wide by 6um long by 0.5um thick bar. Short tethers are included in the simulation. The end face of each tether is mechanically fixed, so that displacement is set to zero. All boundaries are assumed to be thermally insulated.

With these conditions, Femlab is used to mesh the geometry and perform the eigenvalue analysis. Since thermal loss is included in the model, the solutions are complex, and (18) is used to calculate Q.

The eigenvectors contain relative spatial amplitudes, as well as the relative temperature at each node. **Figure 4** shows frames from the longitudinal mode of interest. The mechanical component of the eigenvector is represented by the deformation of the bar, while the thermal component is represented by the shading. As the bar compresses, it heats, with larger temperature amplitude in the center. As the bar stretches, it cools. The simulations yield Q=32,000 at 860 MHz[3] for Aluminum Nitride.

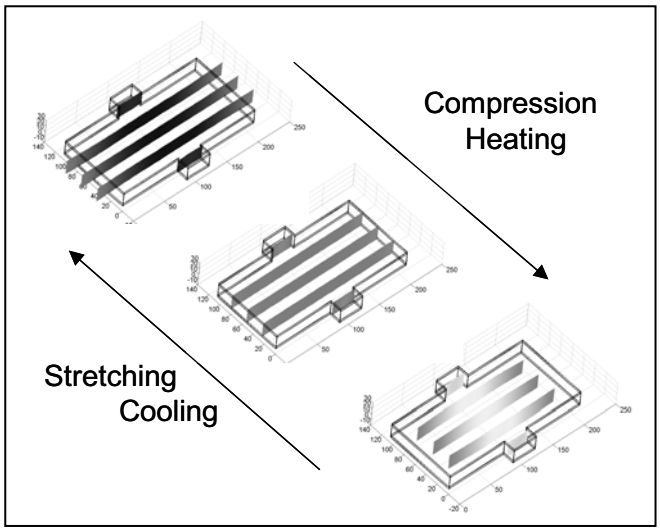

Figure 4: *Frames showing thermoelastic damping longitudinal eigenmode solutions from Femlab.*

This prediction is a powerful tool in optimizing a high Q resonator design, since the effects of material parameters and detailed geometry variations (such as the presence of anchors, fillets, 3-D structure, etc.) can be simulated. In addition, complicated mode structures can be difficult to study analytically. For example, a torsional wave in an infinite medium should not result in thermoelastic damping. However, insightful work by Houston *et al.* [9] considered torsion-type modes in finite geometries and found that the degree of flexural motion associated with the mode could be calculated and used to estimate the quality factor due to thermal losses. The FE eigenvalue analysis can also be used to study this flexural participation effect.

We compared the longitudinal bar Q simulation results to analytical models for thermoelastic damping. A rough estimate for the longitudinal mode Q can be obtained using Zener's formulation, which is nicely outlined in [10]. This analytical approach essentially identifies the uncoupled thermal and mechanical eigensolutions first. The coupling is implemented by identifying the dominant thermal mode that is driven by the strain distribution associated the mechanical resonance of interest. The thermal eigenvalue corresponding to this dominant thermal mode is identified as the characteristic damping time. In

[2] FEMLAB, by Comsol, Inc, is a general purpose partial differential equation solver.

[3] Note that the frequency is higher than the results in Section II. Those simulations included the effective mass of the metal electrodes, thus lowering the frequency, and the Femlab simulations do not.

our longitudinal bar (length L), this thermal time constant is:

$$(19)\quad \tau = \left(\frac{L}{\pi}\right)^2 \frac{C_v}{\kappa}$$

The corresponding Quality factor is [10]:

$$(20)\quad Q^{-1} = \left(\frac{E\alpha^2 T_o}{C_v}\right)\frac{\omega\tau}{1+\omega^2\tau^2}$$

The analytically calculated resonant frequency is:

$$(21)\quad f_o = \frac{1}{2L}\sqrt{\frac{E}{\rho}}$$

For an aluminum nitride bar of length 6um, the above formulas give Q=52,000 at f_o=833 MHz. The simplistic calculation of our mode frequency is different from simulations by about 3.5%, which is to be expected. The Q value, however, is about 1.6 times higher than the simulation result.

Given the ambitious design goals of Q>10^4, including *all* damping effects, accuracy in this prediction can be very important. This necessitates some verification of the simulation approach. A better case study for this verification is a flexural mode resonating beam, since much more rigorous analysis and Q formulas are available for this mode. In reference [4], Lifshitz and Roukes provide a relatively rigorous solution to the coupled thermoelastic beam equations of flexural modes. The approximations made and boundary conditions used are clearly stated. We have used Femlab to simulate the idealized beam (isotropic, made of silicon, with no anchors, etc.) with mechanically fixed and thermally insulating boundaries. The approximations and boundary conditions of the analytical model were implemented in detail. This simulation gave resonant frequencies and Q values that matched [4] to within 8%.

The results of the comparison are shown in **Figure 5**. To explore the thermoelastic effect, Q calculations are presented over a range of frequencies. Frequency is varied by changing the beam width while holding the length-to-width ratio fixed to 10. Thus the fundamental mode frequency is *inversely* proportional to beam width in this experiment. Given the large dynamic range covered in the plot together with the small percent error, it is difficult to see a difference at all. One of the more interesting details observed in conducting this verification was that the analysis used a simplification that temperature flow would be primarily across the flexing beam. (Thus $\nabla^2 T$ was replaced by $\partial^2 T / \partial y^2$). This makes the system more tractable. However, we observed that when we did not include this assumption in the simulation, the deviation between the simulated Q and the calculated Q was systematically large. The deviation grew from only 5% near the Debye peak to as much as 70% at lower frequencies (larger beam widths in **Figure 5**). These observations help to verify the ability of the simulation to reproduce thermoelastic effects in a model system, while they also reinforce the value of using a fully 3D physical model.

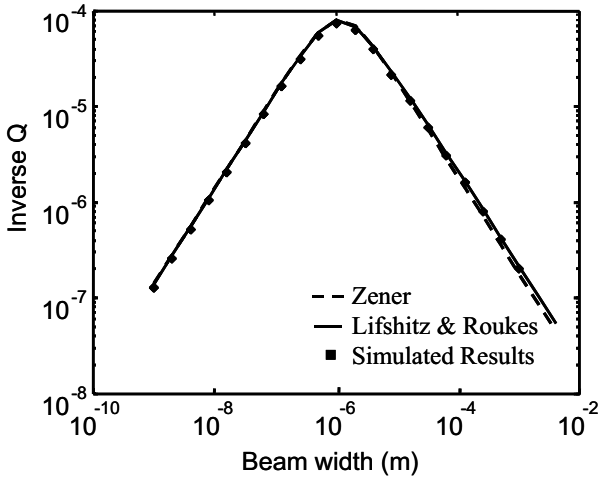

Figure 5: *Quality factor of a thermoelastic beam in fundamental flexural mode. Length-to-width ratio is fixed to 10; thus frequency is inversely proportional to beam width in this plot.*

V. SUMMARY AND CONCLUSIONS

A MEMS piezoelectric resonator has been designed for operation in the GHz frequency range. The design goals of small size, Q>10^4, and impedance at resonance compatible with a 50Ω environment are challenges that were addressed using rigorous modeling tools.

Our contributions to this area include an FE-state space model that obtains an electrical impedance FRF over a wide range of frequencies and can include an arbitrarily large numbers of modes. The FRF obtained on our RF resonator showed that the choice of electrode geometry appropriately isolated our longitudinal mode in the electrical transfer function. We were also able to identify the effects of process imperfections on electrical performance so that we can set appropriate process specifications. Given the impact of the obtaining the electrical FRF, we are currently attempting to automate this using Femlab (in a manner similar to the approach outlined in section IV). Coventor is also currently developing a product targeting piezoelectric MEMS.

We have shown that, given a physical model for the damping in a MEMS resonator, simulations can be used to calculate the Quality factor. The case we studied, thermoelastic damping, is general in the sense that the mechanical constitutive relations for the material are coupled to another internal degree of freedom, in this case temperature. We showed how a complex eigenvalue analysis is used to calculate the Q, and we also showed eigenvectors of the resonant mode, which provides additional intuition. We note that this procedure will work

well for any standard anelastic damping model for which the parameters and boundary conditions can be known. The case studied, thermoelastic damping, is of primary interest to the MEMS community. We provided a validity check for the simulation by comparing to rigorous analytical models of flexural modes. We then applied the tool to cases that are not as accessible analytically, including our own longitudinal mode. We continue to use this simulation approach to study the detailed effects of geometry and materials choices in optimizing our RF resonator for high Quality factor.

APPENDIX: VARIABLE DEFINITIONS

A list of variables, the SI units, and the vector/tensor dimensional structure used in this text is included below.

h = Bar thickness = 0.5 μm.
W = Bar width = 3 μm.
L = Bar Length = 6 μm.
Q = Quality Factor of resonator
n = spatial degrees of freedom (example, 3 : x, y, z)
$\mathbf{u}$ = displacement, meters. nx1 vector.
$\nabla\mathbf{u}$ = nx1 matrix of nx1 vectors
$\mathbf{c}$ = stiffness, N/m. nxn matrix of nxn matrices
$\mathbf{c}\nabla\mathbf{u}$ = nx1 matrix of nx1 matrices
ρ = density, kg/m^3
$\mathbf{e}$ = piezoelectric coefficients, C/m^2.
nxn matrix of nx1 matrices.
ε = dielctric constant, F/m.
V_{in} = input voltage, Volts.
$\mathbf{D}$ = Displacement charge density, C/m^2. nx1 vector
σ_s = Surface charge density, C/m^2
Q_{out} = Output charge on electrode, C
I_{out} = Output current, A
$[\Phi]$ = Matrix of eignevectors
$\{\eta\}$ = Modal amplitudes vector
$\{\tilde{F}\}$ = Modal forcing
$\{\zeta\}$ = Modal damping vector
$\{\omega\}$ = Eigenvalues of state - space solution
$\{\beta\}$ = Generalized modal amplitudes
$\{F\}$ = Force on physical coordinates
$[Q]$ = Operator converting displacement to strain
$[S]$ = Operator sums charge on electrode area
Y = Addmittance Frequency Response Function
Z = Impedance Frequency Response Function
E = Young's modulus
ν = material viscosity
f_o = Resonator frequency of interest. Hz
C_v = Heat capacity at constant volume. J/(K $\cdot$ m^3)
$\boldsymbol{\alpha}$ = coefficient of thermal expansion, 1/$^\circ$C
nx1 matrix of nx1 matrices
κ = thermal conductivity, J/(K $\cdot$ s $\cdot$ m)
$\boldsymbol{\kappa}$ is nx1 matrix of nx1 matrices.
T_o = Nominal Operating Temperature
τ = thermal decay time, seconds

ACKNOWLEDGEMENT

The authors especially thank Mark Mescher and Doug White for valuable conversations and technical guidance. The authors thank Randall Kubena and Deborah Vickers-Kirbey at HRL for helpful conversations. This material is based upon work supported by DARPA under contract #DAAH01-01-C-R204.

REFERENCES

(1) B.A. Auld, Acoustic Fields and Waves in Solids, Vol I, Robert E. Krieger Publishing Co, Inc. (1990).
(2) Theoretical and Experimental Modal Analysis, *Eds* Nuno Manuel Mendes Maia, Júlio Martins Montalvão e Silva, John Wiley & Sons (1997)
(3) D. Salt, Hy-Q Handbook of Quartz Crystal Devices, T.J. Press (Padstow) Ltd. 1987.
(4) R. Lifshitz, M. Roukes, *Phys. Rev. B*, vol 61 no 8, p. 61 (2000).
(5) A. Duwel, J.Gorman, M. Weinstein, J. Borenstein, P. Ward, *Sens and Actuators A*, vol 103, p. 70-75 (2003).
(6) W. Nowaki, Thermoelasticity, Pergamon Press 1986.
(7) C. Zener, *Physical Review* 52, Aug. 1, 1937; p 230.
(8) C. Zener, *Physical Review* 53, Jan. 1, 1938; p 90.
(9) B.H. Houston, D.M. Photiadis, M.H. Marcus, J.A. Bucaro, Xiao Liu, J.F. Vignola, *Appl. Phys. Lett*, vol 80 (7) p. 1300 (2002).
(10) A.S. Nowick, B.S. Berry, Anelastic Relaxation in Crystalline Solids, Ch 17, Academic Press (1972).